Terahertz Band Communications With Topological Valley Photonic Crystal Waveguide

Julian Webber, Yuichiro Yamagami, Guillaume Ducournau, Pascal Szriftgiser, Kei Iyoda, Masayuki Fujita, Tadao Nagatsuma, Ranjan Singh

Terahertz Band Communications With Topological Valley Photonic Crystal Waveguide

Julian Webber, *Senior Member, IEEE*, Yuichiro Yamagami, Guillaume Ducournau, *Member, IEEE*, Pascal Szriftgiser, *Senior Member, IEEE*, Kei Iyoda, Masayuki Fujita, *Member, IEEE*, Tadao Nagatsuma, *Fellow, IEEE*, and Ranjan Singh, *Member, IEEE*

(Invited Paper)

***Abstract*—The sixth generation (6 G) communication standard is expected to include support for very-high data rates (over 100 Gbit/s) and device electronics will require processors with on-chip communications able to support such high bandwidths. Although the terahertz band possesses ample bandwidth, conventional THz waveguides suffer from high bending losses and are sensitive to process defects. The recent revelation of the topological valley photonic crystal (VPC), which exhibits near zero-loss bends, zero back-scattering and zero junction-area, holds much promise for future high speed inter-device communications. Low dispersion in the photonic bandgap region as the number of bends increase is demonstrated through simulation and experiment of the transmission and group delay characteristics. Through comprehensive communications experiments we demonstrate online results below the forward error correction level including an 108-Gbit/s bit rate using multi-level modulation for a 10 mm straight VPC waveguide and a 62.5-Gbit/s bit-rate for a ten sharp bended structure.**

***Index Terms*—Terahertz, topological, valley photonic crystal (VPC), terahertz communications, 6 G, on-chip communication, photonics, UTC-PD, dispersion, waveguide.**

Manuscript received April 6, 2021; revised June 10, 2021; accepted August 9, 2021. Date of publication August 25, 2021; date of current version December 16, 2021. This work was supported in part by the Core Research for Evolutional Science and Technology (CREST) program under Grant JPMJCR1534 of Japan Science and Technology Agency (JST) and KAKENHI budget (Grant- in-Aid for Scientific Research, the Ministry of Education, Culture, Sports, Science and Technology of Japan (MEXT) under Grant 20H01064. This work was supported by the CPER Photonics for Society and DYDICO (Disruptive communications) research cluster of the I-site ULNE and 300 GHz datacom setup was also partially funded by ANR TERASONIC and SPATIOTERA Grants (ANR programs under CE24, 2017 and 2019), and under the TERIL-WAVES project from I-site ULNE and Metropole Européenne de Lille (MEL), 2020. R.S. acknowledges support from Singapore National Research Foundation under Grant CRP23-2019-0005 titled On-Chip Terahertz Topological Photonics for 6G Communication (TERACOMM). *(Corresponding author: Julian Webber.)*

Julian Webber, Yuichiro Yamagami, Kei Iyoda, Masayuki Fujita, and Tadao Nagatsuma are with the Graduate School of Engineering Science, Osaka University, 1-3 Machikaneyama, Toyonaka, Osaka 560-8531, Japan (e-mail: webber@ee.es.osaka-u.ac.jp; u206034e@alumni.osaka-u.ac.jp; u986100d@ecs.osaka-u.ac.jp; fujita@ee.es.osaka-u.ac.jp; nagatuma @ee.es.osaka-u.ac.jp).

Guillaume Ducournau is with the Institut d'Electronique, de Microélectronique et de Nanotechnologie (IEMN), UMR CNRS 8520, Université Lille, Villeneuve d'Ascq, France (e-mail: guillaume.ducournau@univ-lille.fr).

Pascal Szriftgiser is with the Laboratoire de Physique des Lasers Atomes et Molécules (PhLAM), UMR CNRS 8523, Université Lille, F-59655, Villeneuve d'Ascq, France (e-mail: pascal.szriftgiser@univ-lille.fr).

Ranjan Singh is with the Nanyang Technological University, Singapore 639798, Singapore (e-mail: ranjans@ntu.edu.sg).

Color versions of one or more figures in this article are available at https://doi.org/10.1109/JLT.2021.3107682.

Digital Object Identifier 10.1109/JLT.2021.3107682

I. Introduction

THE vast terahertz (THz) band (100 GHz to 10 THz) has received much interest as communications devices and infrastructure are required to support ever increasing data-rates [1] [2]. With the emerging sixth generation (6 G) standard, which is expected to have provision for THz communications, it is expected that the projected data-rates and required bandwidths will continue along a steep trajectory.

Meanwhile emerging communication systems, for example supporting full-resolution mobile-8 K (48 Gbit/s), expect to require processors able to route order of terabit per second data on-chip in extremely small areas. On-chip communication requires support for high bandwidths with both low-loss and low-dispersion despite the routing with several sharp bends. At the same time there is a design trend of increasing the number of cores in the modern central and graphics processing units. As the number of these cores and transistor densities increase, the performances are limited by traditional interconnection methods and THz communications have been proposed as a potential solution e.g. in [3]. The routing is non-trivial even at present densities as for example, a recent network-on-chip architecture that has 64-cores in 32 nm CMOS has a throughput requirement of about 240 Gbit/s [4]. With the ever-higher on-chip signaling-rates there is an expected transition from electronic towards partial and fully photonic circuits.

Although conventional hollow metallic waveguides can exhibit strong field confinement at 300 GHz [5] the manufacturing complexity and cost is significant compared to silicon based waveguides. Metallic waveguiding is less suitable for integration on-chip as it suffers from significant losses with sharp bends [6]. Microstrip waveguide designs can be scaled from microwave to THz frequencies but the ohmic loss is considerable at high frequencies [7]. Photonic crystal (herein referred as 'PC') waveguides provide a convenient platform for development of waveguide structures with low loss compared to conventional metallic waveguides. Confinement in a PC is created by the bandgap in which electromagnetic (EM) waves cannot propagate. In general, the design of a PC has considerable freedom as any material which has a periodic variation in its refractive index will exhibit the bandgap phenomena. The strong bandgap confinement is an attractive feature for highly integrated devices as very small form-factor photonic devices can be developed. A challenge at terahertz frequencies however is that a considerably

larger relative bandwidth is required compared to the nanophotonic devices and very broadband dispersion control is required for the PC [8]. For example, a 30 GHz bandwidth requires a 10% relative bandwidth at 300 GHz while a typical PC exhibits a propagation loss below about 0.5 dB over a relative bandwidth of 7%. Further, this loss increases as the number of bends or their radii of curvature decreases. Topological valley photonic crystal (VPC) [9] waveguides on the other hand have shown near-unity transmission in the photonic bandgap even for sharp bends [10].

The structure of the VPC is fundamentally different to that of the conventional PC which gives it unique properties. A PC has a regular triangular lattice with holes of the same size whereas VPC has a hexagonal lattice with both large and small holes. The PC band gap is created by Bragg reflection while that of VPC is created by breaking the inversion symmetry. Compared to PC the channel and junction losses are decreased as well as the bend or junction area. Topological kink states are able to provide robust, single-mode and linear-dispersion properties. There are inevitable structural imperfections in manufacturing silicon devices due to impurities and in the lithography process which can cause problems for PC based systems especially at high data rates. In this background, VPC possesses very attractive features for building photonic integrated circuits.

Topological photonics have been at the center of intense research over the last 5 years [11], [12]. Recently, the topological phase of light was discovered which potentially can lead to many interesting and useful devices for photonic systems [13], [14]. Photonic topological insulators (PTIs) can be both insulators and conductors at the material edge and offer strong suppression of back-scattering due to large bends and imperfections. A number of PTI applications have been described in the literature for example reflectionless waveguide [15], topological quantum interfaces [16], topological splitters interfaces [17], and robust delay-line [18]. Demonstrations to-date however have mainly been in the microwave e.g. [19] and lightwave frequencies [20] rather than in the THz region. Emitters that are robust to imperfections in the cavity using topological edge states have been developed in [21]–[23] and it is expected to provide revolutionary changes. Schemes for achieving a topological photonic crystal by using dielectric material were described in [24], [25] and a silicon valley-Hall photonic topological insulator was presented in [26]. Experimental demonstrations of VPC at telecommunication wavelengths were described in [27], [28].

We demonstrated the first experimental topological phase of THz wave communication in the 0.3-THz band with an error-free 11 Gbit/s transmission using on-off keying (OOK) modulation for a VPC waveguide with ten sharp bends (zero radii of curvature) comprising five 120-degree and five 60-degree turns [10]. In addition 16-Gbit/s bit-rate was achieved with bit error rate (BER) 1.84×10^{-3} using 16-level quadrature amplitude modulation (QAM). A practical use-case is the wave-guiding of uncompressed 4 K high-definition video that requires 6 Gbit/s error-free signaling [10]. In more recent work, we demonstrated the potential for higher data rates using 16-QAM reporting a 50 Gbit/s result for a 10-bend VPC in [29].

In this paper we demonstrate the markedly higher data-rates of 75 Gbit/s for a 10-bend and 135 Gbit/s for a 10 mm straight structure by employing an intermediate-frequency (IF)-architecture comprising an uni-traveling carrier photodiode (UTC-PD) transmitter (Tx) and sub-harmonic mixer (SHM) receiver (Rx). A study on the transmission and dispersion characteristics and process is additionally made comparing both the straight and with-bend structures.

This paper is organized as follows: The topological VPC design and structure is described in Section II. A study on the transmission and group delay characteristics of the waveguides through simulation is presented in Section III and through experiment in Section IV. Comprehensive communication experiments in the THz band are described in Section V and the performance results are discussed in Section VI. A conclusion of the work is provided in Section VII.

II. Topological Valley Photonic Crystal

One-way edge modes analogous to the quantum Hall effect were first theoretically demonstrated by breaking the time-reversal symmetry of a PC [30]. Importantly, light can be guided unidirectionally without back scattering even in the presence of imperfections and sharp bends due to chiral edge states occurring at the PC perimeter by breaking the symmetry. This phenomena was first demonstrated in the microwave region in [15] and topological protection has since been shown in the optical band regions in [24], [31]–[34]. Creating chiral edge states is a greater challenge in the THz region due to a weak magneto-optical force. Silicon has a large refractive index which results in a large in-plane bandgap while light is maintained in the silicon by total internal reflection and easily exploited in the THz bands using photonic crystals.

A. VPC Design

The VPC is made from high resistivity (>10 k Ω cm) silicon of high relative permittivity (11.7) with a thickness of 200 μ m. VPC has a graphene-like periodic structure composed from unit-cells that in this work have period $a = 242.5$ μm. A unit-cell of the lattice with C_6 symmetry consists of an equilateral triangle hole of edge-length $l_1 = 0.5a$ and a similar inverted equilateral triangle of edge-length $l_2 = 0.5a$. Breaking the symmetry is achieved by increasing edge-length l_1 and reducing the l_2 by an equal amount. In this study we set $l_1 = 0.65a$ and $l_2 = 0.35a$ as depicted in Fig. 1 (a). By breaking the order, the VPC structure has C_3 symmetry and two valleys (at K and K') result that reveal a bandgap from around 320 GHz to 350 GHz [10]. The transverse-electric (TE) modes traverse the *x*-*y* plane while being confined in the *z*-direction by total internal reflection. There are two types of pattern structure termed as 'Small zigzag' as shown in Fig. 1 (b) where the small triangle is closest to the waveguide and 'Large zigzag' where the small triangle is further from the waveguide as shown in Fig. 1 (c). The straight waveguides only employ the Large zigzag interface whereas the bending waveguides include a Large zigzag for the horizontal sections and Small zigzag pattern for the diagonal interface.

The dispersion diagram for the first Brillouin zone showing inside the bandgap with propagation with topological protection under linear dispersion and outside the bandgap with propagation by total internal refraction in straight waveguide is shown in Fig. 2. The red and blue lines represent the edge dispersion, the green regions show the projected bulk dispersion, the yellow dashed line shows the light line which indicates the dispersion of air and the yellow region displays the leaky region where the total-internal refraction condition normal to the slab is not

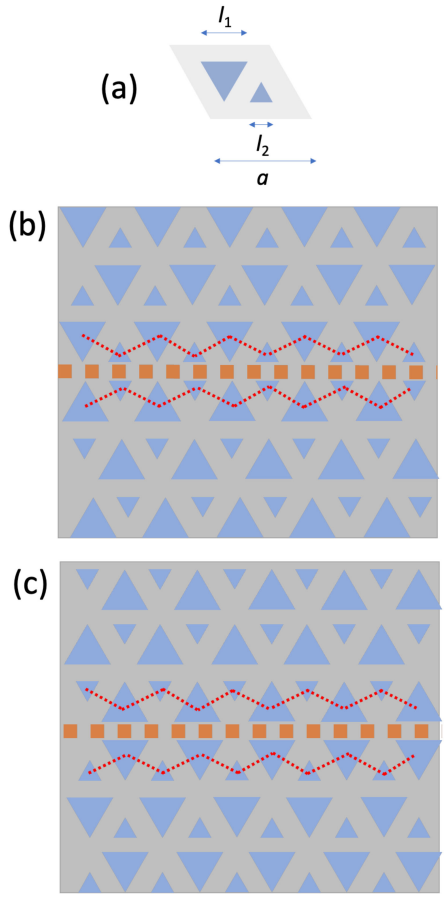

Fig. 1. VPC waveguide structures (a) unit-cell ($a = 242.5$ μm, $l_1 = 0.65a$ and $l_2 = 0.35a$), (b) 'Small zigzag' pattern and (c) 'Large zigzag' pattern.

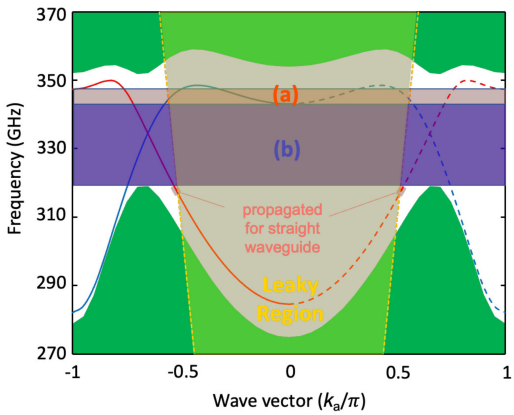

Fig. 2. Dispersion diagram for the first Brillouin zone showing (a) bandgap with linear dispersion for the Large zigzag used in straight sections and (b) bandgap for the Small zigzag additionally employed in the diagonal bend sections. The red and blue lines represent the edge dispersion of Large and Small zigzag waveguides respectively. The light-line in air is indicated by the yellow dashed line.

satisfied. The Small zigzag and Large zigzag patterning impacts on the dispersion and hence usable bandwidth. The bandgap for the Large zigzag is shown by the larger light brown band indicated as (a) while the bandgap for the Small zigzag is shown by the smaller purple band indicated as (b) in Fig. 2. In the

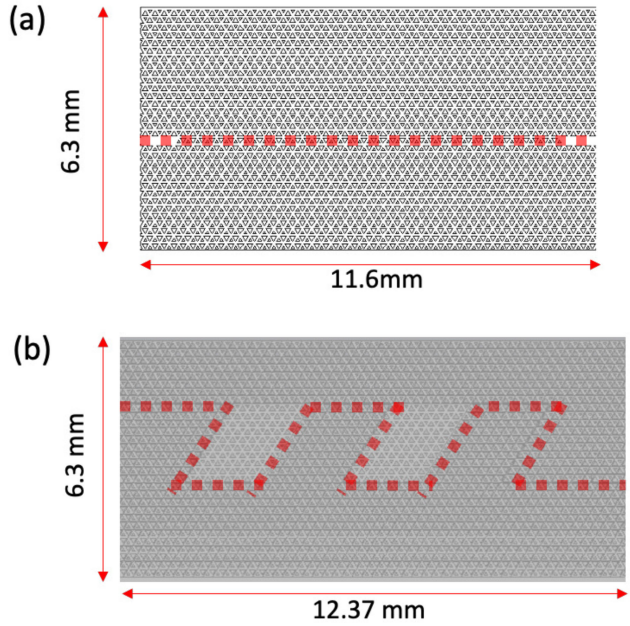

Fig. 3. Schematic of VPC waveguide for (a) 10 mm straight and (b) 10-bends. The dashed red-line indicates the waveguide light path.

straight waveguide case which features the Large zigzag pattern only, the THz wave can propagate in the leaky regions indicated by the yellow color. Signals will couple to the bulk modes with in-plane leakage in the bend structure. In the low frequency region, scattering from the waveguide mode will be coupled to the bulk mode. This leakage into the bulk mode will result in loss and leads to the propagation band for the bend being narrower than that of the straight waveguide. The propagation band of the bend waveguide is reduced to where both bands overlap. From the above results, it is expected the data rate of the 10-bend waveguide will be smaller than that of the straight line.

To experimentally evaluate the performance of the VPC four waveguide specimens were prepared: i) straight 10 mm, ii) straight 30 mm, iii) 10-bend and iv) 18-bend. Of these four, the straight 10 mm and 10-bend were later used in the communications experiments. The VPC straight is a useful waveguide in itself for on-chip communication but it is also used here for comparison with the bend to show the extremely low-losses due to scattering despite the presence of several bends. The ten bend VPC consisted of ten sharp bends (zero radii of curvature) that is five 120 ° and five 60-degree turns as shown in the schematic of Fig. 3. The electric field in the *x*-*y* plane is shown in Fig. 4.

III. Transmission and Dispersion Simulation

In this section we present the results of transmission and dispersion estimation through electromagnetic simulations for the four VPC structures.

A. Transmission

The forward transmission coefficient measures the amplitude and phase from input to output port of the waveguide under test and referred to as the S21 scattering parameter. Here we present the normalized amplitude of each waveguide across the

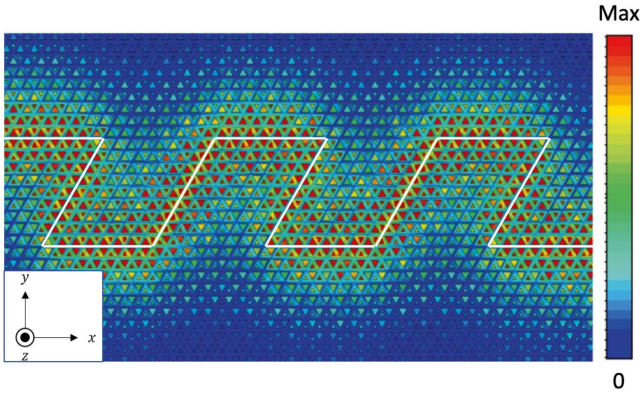

Fig. 4. Electric-field intensity in x-y plane from electromagnetic software simulation.

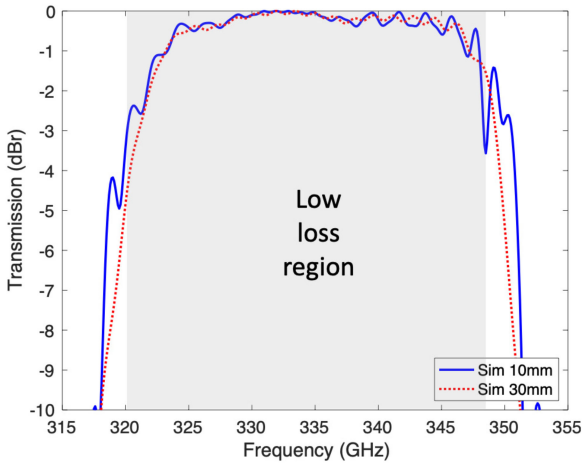

Fig. 5. Transmission from EM simulation for straight 10 mm and 30 mm. The gray area shows the defined low-loss region within the 3-dB bandwidth for the 10 mm straight.

frequency range from 315 GHz to 355 GHz. The S-parameters of each measurement are normalized so the maximum amplitude across the frequency range is plotted as unity or zero dB. The y-scale is then expressed in dBr (decibel relative) units and allows the 3-dB bandwidth of each waveguide to be easily compared. VPC exhibits extremely low channel-loss (we experimentally measured this to be between 0.0015–0.05 dB/mm in [10]) and the 3-dB bandwidth is a parameter heavily influencing the relative performances of short-distance on-chip communication.

The transmission for straight 10 mm and 30 mm in simulation is shown in Fig. 5. The large band gap extending from about 320 GHz to 348 GHz can be seen with near unity transmission. We define a low-loss region shown in gray for the 10 mm straight in Fig. 5 as that within the 3-dB bandwidth. The transmission for 10-bend and 18-bend is shown in Fig. 6. A similar very low-loss region in the band gap is observed for the bent structure in Fig. 6 with near unity transmission and very low loss estimated at $<$0.1 dB / bend. However the transmission is affected in the high frequency band due to the pronounced dip observed at around 344 GHz. The two low-loss regions are also shown in subsequent figures discussing the gain and dispersion in experiment.

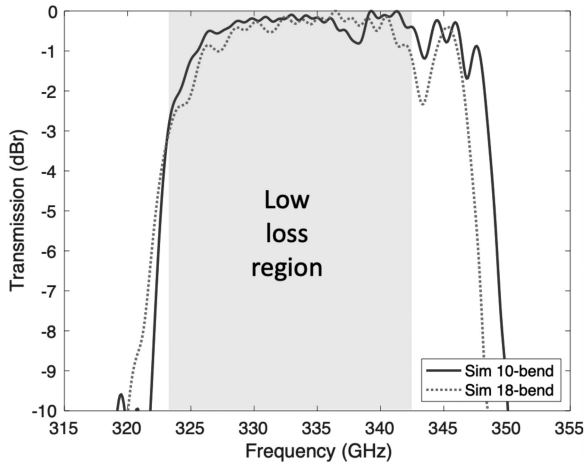

Fig. 6. Transmission from EM simulation for 10-bend and 18-bend. The low-loss region is defined within the 3-dB bandwidth in the low frequency band and is limited in the high frequency by the dip at about 344 GHz.

B. VPC Fabrication Tolerance

Due to its topological properties VPC is generally robust to imperfections in the fabrication or manufacturing process. We have shown that when large and small cells are randomly swapped the 3-dB bandwidth decreases by about 0.75 GHz [10]. The 3-dB bandwidth decreased by about 2 GHz when air hole sizes were randomly increased or decreased by 20% in a central hexagon covering about 12 cells centered on the waveguide interface [10]. These results were consistent with those reported in [9]. In a further simulation, the sizes of the small cells at the domain interface were set randomly from $0.35a$-$w/2$ to $0.35a$+$w/2$ and the sizes of the larger cells were similarly varied between $0.65a$-$w/2$ to $0.65a$+$w/2$ where w indicates the disorder strength. It was shown through a Monte-Carlo simulation that when $w<$ 0.3 there is minimal impact on the gain in the band gap but transmission decreases rapidly for $w\geq$ 0.3 due to the inter-valley scattering effects [10].

In addition, we have modeled the effect of a constant (-5, -2.5, 0, 2.5, 5) % error in the lengths of both l_1 and l_2 for all cells on the 3-dB bandwidth. That is, $l_1 = 0.35av$, $l_2 = 0.65av$, where v is an error-scaling factor to model the departure from the desired value of one. A constant error for all cells models the effect of machine tool tolerance that creates cells with a constant size different to that set. The results show that the 3-dB bandwidth changes by (-1.5, -0.8, 0, 0.5, 7) dB as v changes from (0.95, 0.975, 1.0, 1.025, 1.05) respectively. Practical size errors are likely to be normally distributed and centered on zero with a small variance and these results therefore represent the more extreme case.

The collective results of all simulations indicate that typical fabrication tolerances are unlikely to significantly impact on the robustness of the VPC.

C. Group Delay

A signal can be transmitted through a waveguide on a number of different modes and each mode has a slightly different time of arrival leading to group velocity variation resulting in dispersion and ultimately limiting the effective bandwidth for

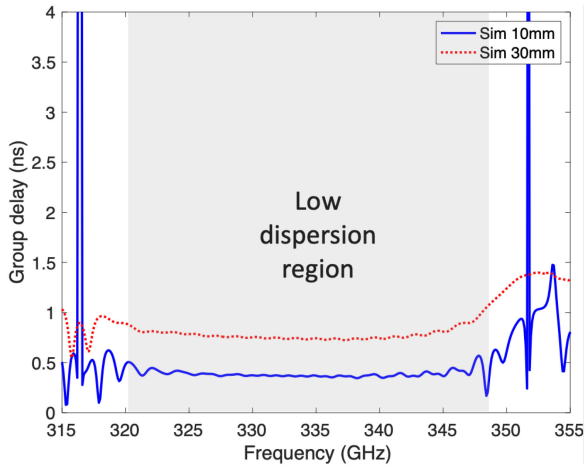

Fig. 7. Group delay from EM simulation for straight 10 mm and 30 mm. The low-dispersion region is in agreement with the low-loss region in Fig. 5.

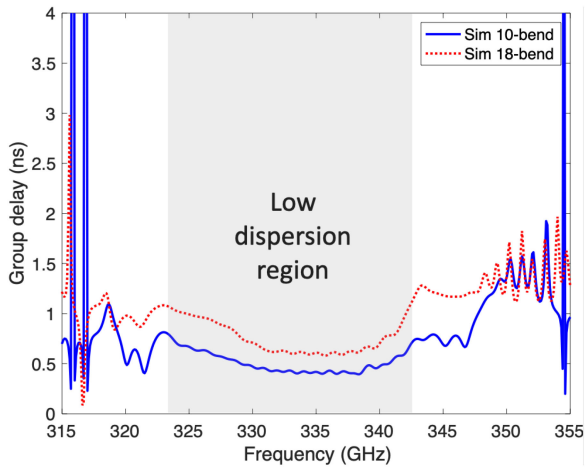

Fig. 8. Group delay from EM simulation for 10-bend and 18-bend. The low-dispersion region is in agreement with the low-loss region in Fig. 6.

communications. Signal components are delayed by different amounts due to the channel frequency selectivity which leads to phase distortion. The group delay is the time taken as a function of frequency for a signal to travel through the waveguide. In the ideal channel with zero group delay the phase will linearly change with frequency after phase unwrapping and the gradient with respect to frequency (1) will be flat.

$$GD = \frac{-\delta\psi}{\delta\omega} \tag{1}$$

where $\delta\psi$ is the change in phase (radians) and $\delta\omega$ is the change in angular frequency. The simulated group delay for straight 10 mm and 30 mm in simulation is shown in Fig. 7. The delay is about 0.5 ns across the low-dispersion region as constructed from the transmission data. The dispersion increases by about 0.4 ns for the longer 30 mm sample. The group delay for the 10-bend and 18-bend are compared in Fig. 8. The delay increases by about 0.25 to 0.4 ns for the 18-bend which is comparable to the increase seen with the short and long straight waveguides. We can see there is limited additional impact from the bend in the photonic band gap region and the additional delay seen at the low

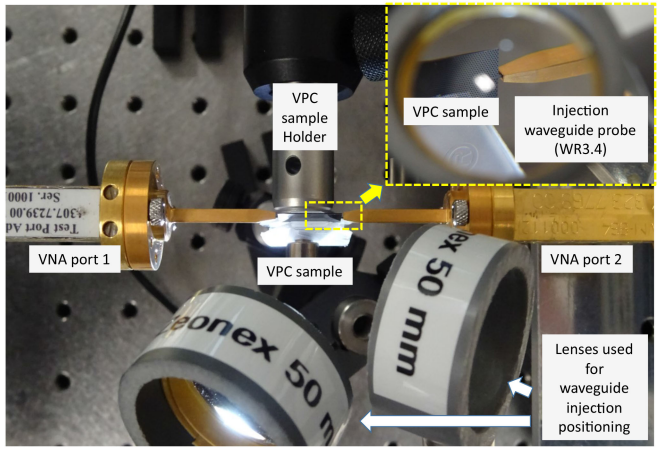

Fig. 9. View showing experiment setup during the VNA measurement of the VPC devices. Waveguide probes are connected to the VNA port as seen in the center left and right. (Inset) The magnifying lens helps in the centering of the VPC taper in the waveguide probe.

frequency edge for the bend is considered due to the coupling of energy into the bulk modes. The difference in group velocity resulting from the large and small triangle may also have some impact.

IV. Transmission and Dispersion Experiment

In this section we report on the transmission and dispersion estimation based on measurements obtained by a vector network analyzer (VNA). The VNA measurement was achieved in two steps from 220–330 GHz (WR3.4) and 325–500 GHz (WR2.2). In each case, the VNA was waveguide-calibrated using a set of Thru / Reflect / Match standards (TRM calibration procedure), for both WR3.4 and WR2.2 bands. A photograph of the experiment setup during the VNA measurement of the VPC devices is shown in Fig. 9. The waveguide taper of width 210 μm is centered into the waveguide probe with assistance of a magnifying lens for aligning the 3-axes.

A. Transmission

The S21 transmission for straight 10 mm and 30 mm is shown in Fig. 10. The distinct bandgap can be seen in the figures extending from 320–350 GHz and sharp attenuation outside. The gray low-loss region that was generated from the simulation in Fig. 5 is shown. Although there is some loss in transmission observed in the center of the low-loss region it is small enough not to impact on the 3-dB bandwidth. A part of the small loss seen as ripple in the low loss region could be attributed to potential misalignment of the taper and WR3.4 / WR2.2 waveguides as well as between the taper and body itself which will result in mode and impedance mismatching. The 3-dB-bandwidth is computed as 29.5 GHz for the 10 mm straight. The transmission for 10-bend and 18-bend is shown in Fig. 11 and extends from about 323–348 GHz. The transmittance band of the bent waveguide is slightly reduced at the lower frequency and this is conjectured to be due to a coupling from the waveguide mode to the bulk mode at the bend whereas total internal reflections occur for the straight waveguide. The transmission is complex outside the band gap with signs of more random behavior due to

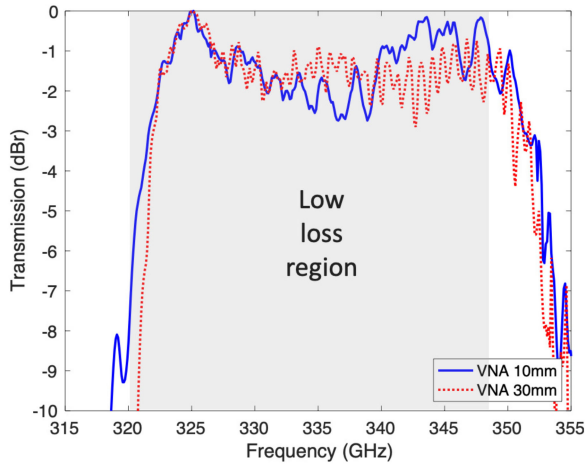

Fig. 10. Transmission from VNA measurement for straight 10 mm and 30 mm. The gray low-loss region is as defined from the simulation in Fig. 5.

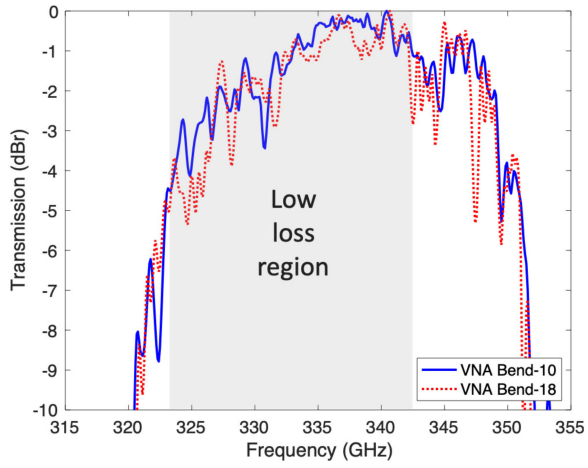

Fig. 11. Transmission from VNA measurement for 10-bend and 18-bend. The gray low-loss region is as defined in Fig. 6.

TABLE I
MEASURED 3-DB BANDWIDTH RESULTS

Type	$f_{low-3dB}$	$f_{high-3dB}$	3-dB BW
Straight-10mm	321.6 GHz	351.2 GHz	29.6 GHz
Straight-30mm	322.0 GHz	350.3 GHz	28.3 GHz
10-bend	330.9 GHz	349.2 GHz	18.3 GHz
18-bend	326.0 GHz	344.1 GHz	18.1 GHz

the combined processes of reflection and refraction of the THz wave occurring at the boundaries of the VPC and at the domain wall [33], [35]. It can be seen that the bending loss is small as the number of bends increase in the low dispersion band. The 3-dB bandwidth is calculated as 18.3 GHz for the 10-bend and corresponds to the photonic band gap region. It can be seen there is a narrow dip of about 3.4 dB between 330.6–330.8 GHz without which the bandwidth would have been measured at 23.8 GHz and it is possible that this dip is due to a slight measurement misalignment. The four 3-dB bandwidths are summarized in Table I.

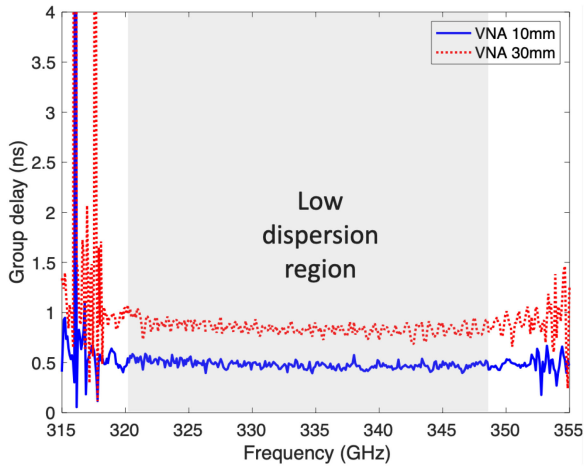

Fig. 12. Group delay from VNA measurement for straight 10 mm and 30 mm. The gray low-dispersion region is as defined from the simulation result in Fig. 7.

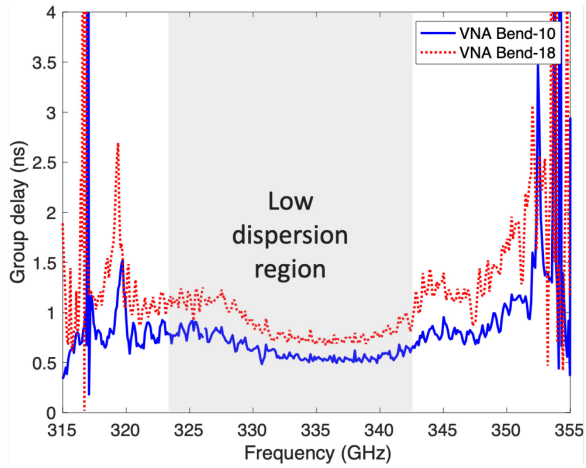

Fig. 13. Group delay from VNA measurement for 10-bend and 18-bend. The gray low-dispersion region is as defined from the simulation result in Fig. 8.

B. Group Delay

The computed group delay from complex phase data measured on VNA for straight 10 mm and 30 mm is shown in Fig. 12 where the gray low-dispersion region is as defined from the simulation result in Fig. 7. An increase in delay of about 0.4 ns is observed for the longer waveguide. The linear dispersion indicates a negligible signal delay across a range of frequencies, resulting in a larger usable bandwidth [36]. The group delay for the 10-bend and 18-bend waveguide is shown in Fig. 13. The gray low-dispersion region is as defined from the simulation in Fig. 8. The low group delay over the bandgap is apparent for both the straight as well as 10-bend structure. The average value of group delay in the bandgap center at 336 GHz was about 0.5 ns and 0.52 ns for the straight and 10-bend structures respectively. The group delay increases by an average of only about 0.3 ns within the low dispersion region despite the addition of eight bends and this increase is less than that observed when comparing the short and long straight waveguides.

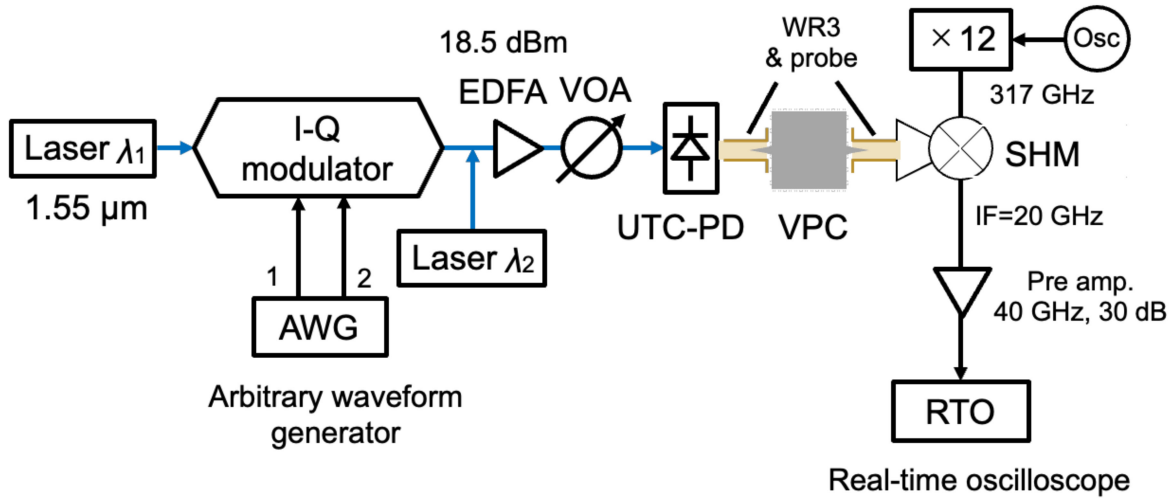

Fig. 14. Block diagram of the I-Q communications experiment. The VPC waveguide tapers interface between the uni-traveling carrier-photodiode (UTC-PD) Tx and sub-harmonic mixer (SHM) receiver using probe extenders.

V. Communications Experiment Set-Up

Very high data-rate communication is one of the attractive features of THz based systems. In this section we describe the hardware set-up for experiments to achieve our highest data-rates to-date. Two experiment configurations were set-up for: i) complex I-Q modulation and ii) amplitude shift keying (ASK) modulation.

A. Complex Modulation

The block diagram of the I-Q communication experiment set-up is shown in Fig. 14. Complex data signals were generated by an arbitrary waveform generator (AWG) with 5 samples per symbol. The signal stream was pulse-shaped to minimize the inter-symbol interference (ISI) by filtering with a root-raised cosine (RRC) filter with roll-off factor, $\alpha = 0.35$. The roll-off factor determines the amount of excess-bandwidth over Nyquist that is used for transmission [37]. An alpha of zero represents the brick-wall filter and $\alpha = 0.35$ is a common value that is a compromise between limiting the transmission bandwidth and the increase in ISI.

The filtered signal was modulated on to light using a complex I-Q modulator. The resulting optical signal was then amplified by an erbium doped fiber amplifier (EDFA) to about 18.5 dBm, passed through a polarization controller, voltage controlled attenuator, and THz waves generated using a UTC-PD. The UTC-PD contains a photodiode that converts the optical signal to an electrical terahertz band signal. UTC-PD have strong potential to down-convert advanced modulation formats from optical to THz domain, for up to 100 Gbit/s links [38]. The VPC input port taper was inserted into a probe extender that connected to the UTC-PD via hollow waveguide on the Tx side. The VPC output port taper was interfaced to the SHM by an identical probe arrangement on the Rx side.

The SHM was pumped to operate at 317 GHz and the down-converted signal was centered at an intermediate frequency (IF) of 20 GHz. The IF signal was post-amplified using a 40 GHz bandwidth pre-amplifier, then converted to baseband using digital signal processing (DSP) software running on a real-time oscilloscope (RTO). The I-Q modulator bias was set by a two-dimensional search routine with feedback from the DSP software to provide an optimized value. A matched RRC filter was applied at the Rx resulting in a combined raised cosine filtering response.

B. Amplitude Modulation

The ASK modulation experiment followed the complex modulation measurements with some changes to principle component. A pseudo random bit sequence signal was generated by the AWG and Nyquist filtered. The data was modulated using a standard intensity modulator in place of the I-Q modulator. The modulated light-carrier was amplified using the EDFA and the optical power controlled by the VOA prior to transmission using the UTC-PD as in the case of complex modulation. The VPC 10-bend sample was interfaced to the Tx and Rx using the same method as in the I-Q experiment. After envelope detection at the Rx the signal is amplified and signal conditioned using a limiting-amplifier. The pre-amplifier output and limiting-amplifier output eye diagrams for the 10 Gbit/s ASK modulation signal are shown in Fig. 15 (top) and (bottom) respectively. The conditioned signal is then matched filtered, equalized and a real time BER measurement made.

VI. Communications Experiment Results

A comprehensive communications measurement campaign (80 tests in total) were conducted each with one or more different settings for the VPC structure, modulation, and UTC-PD photocurrent. For each setting the error-vector magnitude (EVM), BER performance, signal to noise ratio (SNR) and I-Q constellation plot were recorded. Here we present the key performance results.

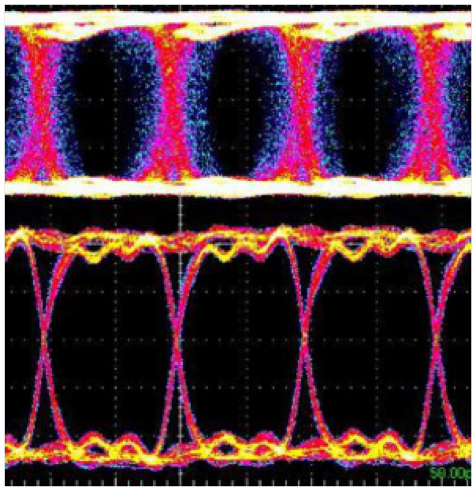

Fig. 15. Eye-diagrams at (top) pre-amplifier output and (bottom) limiting-amplifier output for 10 Gbit/s ASK modulation.

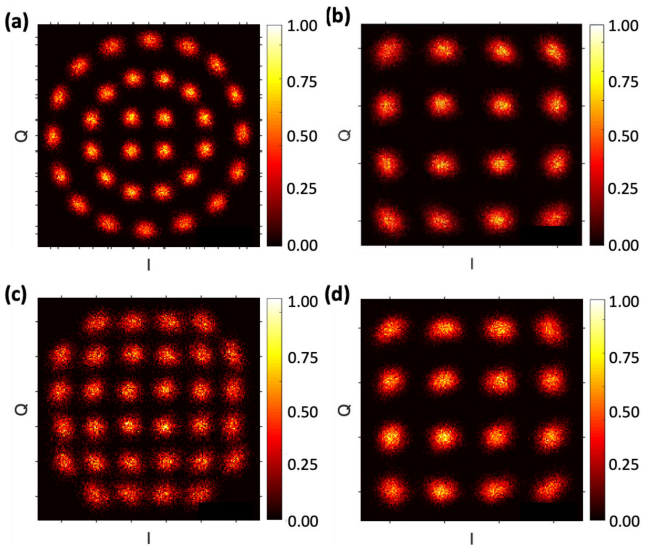

Fig. 16. I-Q intensity constellation diagram for recovered symbols: 10 mm straight at (a) 100 Gbit/s using 32-APSK, (b) 100 Gbit/s using 16-QAM, (c) 125 Gbit/s using 32-QAM and (d) 108 Gbit/s using 16-QAM. The intensity scale on the right indicates the 3-dimensional distribution of I-Q points over multiple frames.

A. I-Q Intensity Diagrams

The I-Q diagram plot shows the detected symbols after channel equalization and prior to symbol demapping into data bits. When plotting the constellation over multiple frames the intensity scale indicates the 3-dimensional distribution of I-Q points. The I-Q intensity constellation diagrams for recovered symbols for 10 mm straight at (a) 100 Gbit/s, using 32-level amplitude phase shift keying (32-APSK) and 20 GBaud, (b) 100 Gbit/s, using 16-QAM (25 GBaud), (c) 125 Gbit/s using 32-QAM (25 GBaud) and (d) 108 Gbit/s using 16-QAM (27 GBaud) are shown in Fig. 16. The clearly defined constellation points show the sufficient SNR level, system fidelity as well as good performance of the software based DSP equalization. Meanwhile I-Q constellation diagrams for 10-bend at (a) 60 Gbit/s using 64-QAM (10 GBaud), (b) 60 Gbit/s using 32-APSK (12 GBaud), (c) 75 Gbit/s using 64-QAM (12.5 GBaud) and (d) 50 Gbit/s using 16-QAM (12.5 GBaud) are shown in Fig. 17.

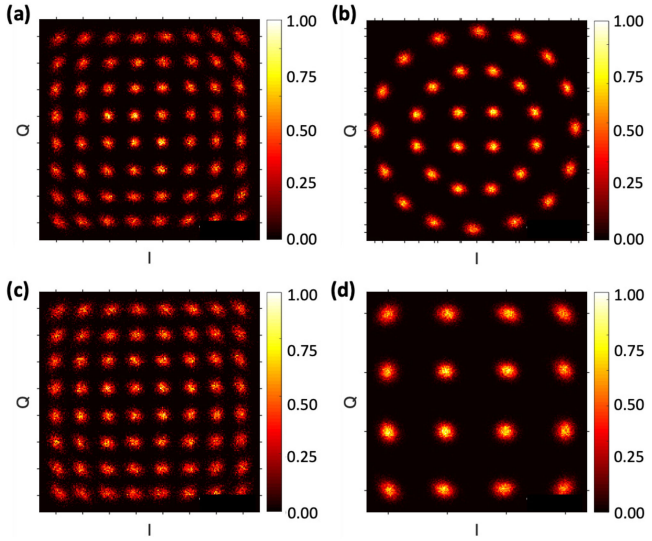

Fig. 17. I-Q intensity constellation diagram for recovered symbols: for 10-bend (a) 60 Gbit/s using 64-QAM, (b) 60 Gbit/s using 32-APSK, (c) 75 Gbit/s using 64-QAM, and (d) 50 Gbit/s using 16-QAM. The intensity scale on the right indicates the 3-dimensional distribution of I-Q points over multiple frames.

B. Error Vector Magnitude

EVM is a performance measure of the demodulator in the presence of interference and noise. Specifically it is the difference between the ideal transmitted symbol and the recovered baseband symbol. Impairments such as phase noise, I-Q imbalance, non-linearity and distortion from filters all contribute to an increased EVM. The on-line demodulator software reports the root mean square (rms) percentage EVM which is defined as (2)

$$EVM = \sqrt{\frac{\sum_{k=0}^{N-1} |E(k)|^2}{\sum_{k=0}^{N-1} |S(k)|^2}} \tag{2}$$

where $E(K)$ is the error signal and $S(K)$ is the Tx or reference signal, N is the number of symbols, and k is the symbol index.

EVM versus Tx relative power for 50 Gbit/s straight 10 mm and 10-bend are shown in Fig. 18. It can be seen that the EVM steadily decreased with log increase in the Tx power increased but a floor eventually appeared to be reached at about 9% for the 100 Gbit/s straight. Very low EVM was recorded at signaling data-rates. For example the EVM was 3.8% for 32-QAM at 40 Gbit/s and 3.8% for 64-QAM at 48 Gbit/s was achieved for the 10-bend structure. Note an rms EVM of 9% is considered normal for a mobile station with limited analog to digital converter (ADC) quantization and 10% an extreme case in microwave communications [39]. In the case of a base-station with higher resolution ADC and high performance radio frequency (RF) front-end the normal EVM range is 7-8%.

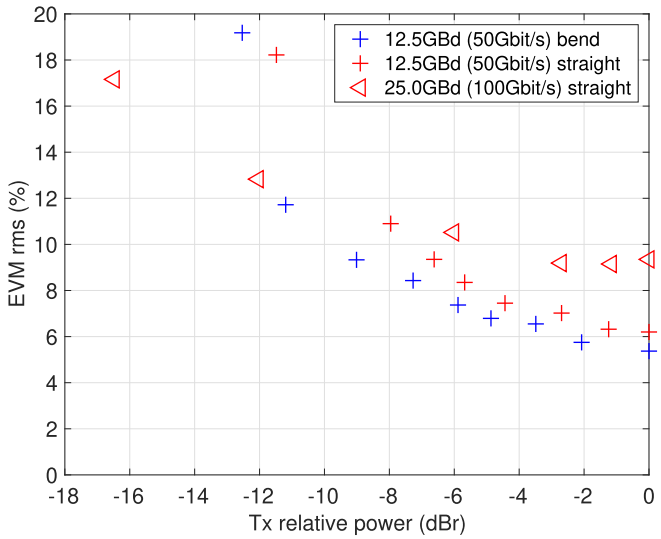

Fig. 18. EVM versus Tx relative power for straight 10 mm and 10-bend.

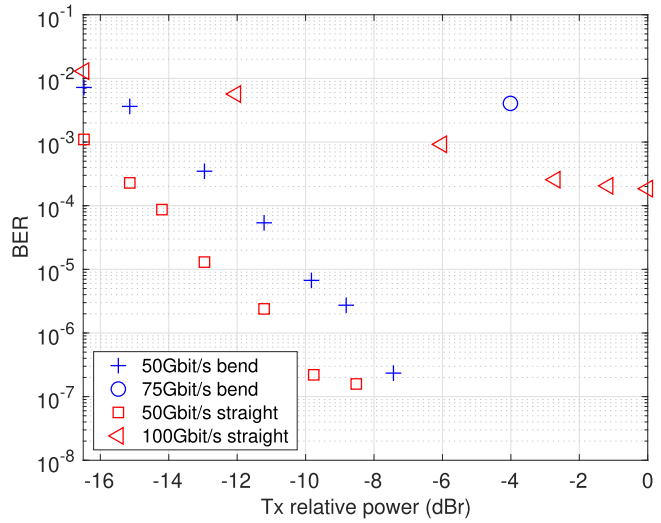

Fig. 19. BER versus Tx relative power for straight 10 mm and 10-bend using I-Q modulation.

C. Data-Rate and BER Performance

In general employing the higher order modulation allowed the higher data-rates to be achieved subject to the EVM being below a threshold to enable detection with acceptable BER. Errors can be corrected if their frequency is below the forward-error correction (FEC)-recoverable rate. As the I-Q constellation points get closer together the error-rate increases and 64-QAM modulation could be decoded at the maximum symbol rate of 16 GBaud. The BER versus Tx relative power for the straight and 10-bend is presented in Fig. 19. The Tx power for all configurations is normalized to the highest Tx current of 4 mA. That is 0 dBr corresponds to the Tx current of 4 mA. In the case of the straight waveguide it can be seen that 100 Gbit/s was achieved at 1.85×10^{-4} and below the FEC-level. For the 10-bend structure we were able to decode data at 75 Gbit/s for sufficiently high Tx power. For both the straight and 10-bend

TABLE II
KEY STRAIGHT 10 MM PERFORMANCE RESULTS. ([*] INDICATES ABOVE THE FEC-LEVEL OF 2×10^{-3})

Data rate	Symbol rate	Modulation	BER
135 Gbit/s	27 GBd	32-QAM	1.73×10^{-2} [*]
125 Gbit/s	25 GBd	32-QAM	1.14×10^{-2} [*]
108 Gbit/s	27 GBd	16-QAM	7.40×10^{-4}
100 Gbit/s	25 GBd	16-QAM	1.85×10^{-4}
100 Gbit/s	20 GBd	32-APSK	2.1×10^{-3} [*]
80 Gbit/s	20 GBd	16-QAM	7.50×10^{-6}
50 Gbit/s	12.5 GBd	16-QAM	1.58×10^{-7}

TABLE III
KEY 10-BEND PERFORMANCE RESULTS ([*] INDICATES ABOVE THE FEC-LEVEL OF 2×10^{-3})

Data rate	Symbol rate	Modulation	BER
75 Gbit/s	12.5 GBd	64-QAM	4.05×10^{-3} [*]
62.5 Gbit/s	12.5 GBd	32-APSK	1.75×10^{-4}
62.5 Gbit/s	12.5 GBd	32-QAM	1.14×10^{-4}
60 Gbit/s	10 GBd	64-QAM	1.83×10^{-3}
50 Gbit/s	12.5 GBd	16-QAM	2.34×10^{-7}

at 50 Gbit/s the log BER reduced approximately linearly with the log increase in Tx power and very low error rates were achieved.

Whether a symbol is recoverable however depends on if the errors occur in clusters or are evenly distributed and also on the type of error correction and the coding rate. In this work we consider a commonly used value for the FEC rate of 2×10^{-3} [40] and assume codes are used in the absence of long error bursts with about a 7% code overhead. Recovery may be possible at higher error-rates by using different codes or a higher code overhead.

Higher order QAM enables high bandwidth efficiency but is susceptible to noise and requires more complex hardware than systems such as OOK. Amplifier linearity is also important due to bits being encoded on an amplitude component. APSK is more robust to nonlinear distortions compared to QAM signals due to its circular constellation characteristic and is commonly employed in the Digital Video Broadcasting - Satellite - Second Generation (DVB-S2) standard system [41]. APSK-16 consists of two concentric rings of equally spaced 4, 12 PSK points while APSK-32 constellation adds an additional outer ring of 16 PSK points.

The highest data-rate inside the FEC rate for the 10 mm straight was 108 Gbit/s realized using 27 GBd signaling at an error rate of 7.4×10^{-4}. The highest data-rate above the FEC level for the 10 mm straight was 135 Gbit/s corresponding to 27 GBaud employing 32-APSK modulation and realized with the BER of 1.73×10^{-2}. The bit-rate of 62.5 Gbit/s was achieved with BER of 1.14×10^{-4} while 75 Gbit/s could be achieved at BER of 4.05×10^{-3} for the 10-bend design. The key performances of the straight 10 mm and 10-bend devices are summarized in Table II and Table III respectively.

The BER versus relative detected power from the ASK modulation experiment is plotted in Fig. 20. The result shows that error-free (below 1×10^{-11}) communications could be achieved at the maximum detected power for this experiment. The NRZ baseband signaling at 10 Gbit/s should require about 14-15 GHz

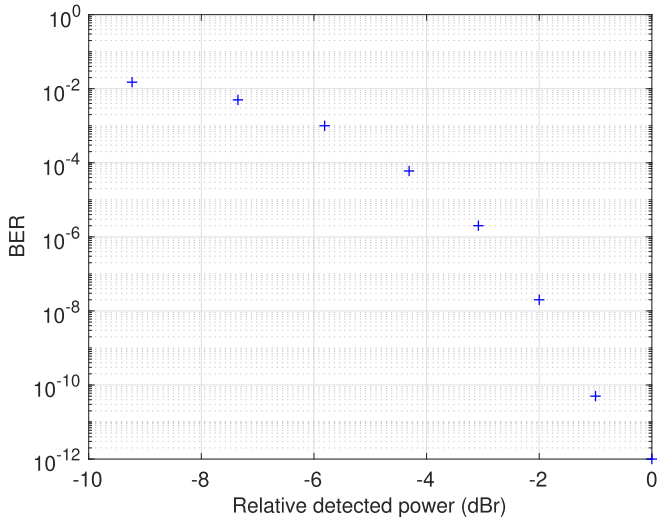

Fig. 20. BER versus Tx relative power for 10-bend at 10 Gbit/s data-rate using amplitude shift keying modulation.

of RF bandwidth and this requirement could be achieved within the low dispersion band of the 10-bend sample.

VII. Conclusion

Data-rates of 108 Gbit/s and 62.5 Gbit/s were respectively achieved below the FEC-level for the 10 mm straight and ten-bend structures using complex modulation while error-free communications were demonstrated at 10 Gbit/s using amplitude modulation. The transmission band of the bending waveguide occurs inside the photonic bandgap whereas the THz wave is propagated in the waveguide mode with total internal reflection for the straight waveguide. This indicates that an increase in the bandwidth of photonic bandgap is required for higher data rates with the bending structure. Nevertheless the simulations and experimental results have shown the minimal increase in dispersion in the bandgap region as the number of bends increase other than that due to the increase in length.

Optimization of the waveguide structure with different zigzag patterns is an area of ongoing research in order to increase the usable bandwidth and extend the data-rate. The integration of resonant tunneling diodes (e.g. see [42], [43]) and development of branch and diplexer devices are also our future perspective.

References

[1] M. Tonouchi, "Cutting-edge terahertz technology," *Nature Photon.*, vol. 1, no. 2, pp. 97–105, 2007.
[2] T. Nagatsuma, G. Ducournau, and C. Renaud, "Advances in terahertz communications accelerated by photonics," *Nature Photon.*, vol. 10, no. 6, pp. 371–379, 2016.
[3] S. Saxena, D. Manur, N. Mansoor, and A. Ganguly, "Scalable and energy efficient wireless inter chip interconnection fabrics using THz-band antennas," *J. Parallel Distrib. Comput.*, vol. 139, pp. 148–160, 2020.
[4] Y. Chen and C. Han, "Channel modeling and characterization for wireless networks-on-chip communications in the millimeter wave and terahertz bands," *IEEE Trans. Molecular, Biol. Multi-Scale Commun.*, vol. 5, no. 1, pp. 30–43, Oct. 2019.
[5] A. von Bieren, E. De Rijk, J.-P. Ansermet, and A. Macor, "Monolithic metal-coated plastic components for mm-wave applications," in *Proc. Int. Conf. Infrared, Millimeter, Terahertz Waves*, 2014, pp. 14–19.
[6] K. Wang and D. Mittleman, "Metal wires for terahertz wave guiding," *Nature*, vol. 432, no. 7015, pp. 376–379, 2004.
[7] K. R. Jha and G. Singh, "Analysis of narrow terahertz microstrip transmission-line on multilayered substrate," *J. Comput. Electron.*, vol. 10, no. 1-2, pp. 186–194, 2011.
[8] X. Yu, M. Fujita, and T. Nagatsuma, "Simultaneous low-loss and low-dispersion in a photonic-crystal waveguide for terahertz communications," *Appl. Phys. Exp.*, vol. 12, no. 1, 2019, Art. no. 012005.
[9] X. He *et al.*, "A silicon-on-insulator slab for topological valley transport," *Nature Commun.*, vol. 10, no. 1, pp. 1–9, 2019.
[10] Y. Yang *et al.*, "Terahertz topological photonics for on-chip communication," *Nature Photon.*, vol. 14, no. 7, pp. 446–451, 2020.
[11] T. Ozawa, H. M. Price, A. Amo, N. Goldman, and M. Hafezi *et al.*, "Topological photonics," *Rev. Modern Phys.*, vol. 91, no. 1, 2019, Art. no. 015006.
[12] S. Iwamoto, Y. Ota, and Y. Arakawa, "Recent progress in topological waveguides and nanocavities in a semiconductor photonic crystal platform," *Opt. Mater. Exp.*, vol. 11, no. 2, pp. 319–337, 2021.
[13] L. Lu, J. D. Joannopoulos, and M. Soljačić, "Topological photonics," *Nature Photon.*, vol. 8, no. 11, pp. 821–829, 2014.
[14] A. B. Khanikaev and G. Shvets, "Two-dimensional topological photonics," *Nature Photon.*, vol. 11, no. 12, pp. 763–773, 2017.
[15] Z. Wang, Y. Chong, J. Joannopoulos, and M. Soljačić, "Observation of unidirectional backscattering-immune topological electromagnetic states," *Nature*, vol. 461, no. 7265, pp. 772–775, 2009.
[16] S. Barik *et al.*, "A topological quantum optics interface," *Science*, vol. 359, no. 6376, pp. 666–668, 2018.
[17] Y. Yang *et al.*, "Realization of a three-dimensional photonic topological insulator," *Nature*, vol. 565, no. 7741, pp. 622–626, 2019.
[18] M. Hafezi, E. A. Demler, M. D. Lukin, and J. M. Taylor, "Robust optical delay lines with topological protection," *Nature Phys.*, vol. 7, no. 11, pp. 907–912, 2011.
[19] X. Cheng, C. Jouvaud, X. Ni, S. Mousavi, A. Genack, and A. Khanikaev, "Robust reconfigurable electromagnetic pathways within a photonic topological insulator," *Nature Mater.*, vol. 15, no. 5, pp. 542–548, 2016.
[20] B. Bahari *et al.*, "Nonreciprocal lasing in topological cavities of arbitrary geometries," *Science*, vol. 358, no. 6363, pp. 636–640, 2017.
[21] Y. Ota *et al.*, "Photonic crystal nanocavity based on a topological corner state," *Optica*, vol. 6, no. 6, pp. 786–789, 2019.
[22] P. St-Jean *et al.*, "Lasing in topological edge states of a one-dimensional lattice," *Nature Photon.*, vol. 11, no. 10, pp. 651–656, 2017.
[23] M. A. Bandres *et al.*, "Topological insulator laser: Experiments," *Science*, vol. 359, no. 6381, pp. 1–5, Mar. 2018.
[24] L. Wu and X. Hu, "Scheme for achieving a topological photonic crystal by using dielectric material," *Phys. Rev. Lett.*, vol. 114, no. 22, 2015, Art. no. 223901.
[25] H. Kagami, T. Amemiya, S. Okada, N. Nishiyama, and X. Hu, "Topological converter for high-efficiency coupling between Si wire waveguide and topological waveguide," *Opt. Exp.*, vol. 28, no. 22, pp. 33619–33631, 2020.
[26] T. Ma and G. Shvets, "All-Si valley-hall photonic topological insulator," *New J. Phys.*, vol. 18, no. 2, 2016, Art. no. 025012.
[27] M. Shalaev, W. Walasik, and N. M. Litchinitser, "Experimental demonstration of valley-hall topological photonic crystal at telecommunication wavelengths," in *CLEO QELS Fundam. Sci.*, OSA, 2018, p. FM4Q-3.
[28] T. Yamaguchi *et al.*, "GaAs valley photonic crystal waveguide with light-emitting InAs quantum dots," *Appl. Phys. Exp.*, vol. 12, no. 6, 2019, Art. no. 062005.
[29] J. Webber, Y. Yamagami, G. Ducournau, M. Fujita, T. Nagatsuma, and R. Singh, "50-Gbit/s terahertz communication using a valley photonic crystal waveguide," *Int. Conf. Infrared, Millimeter, Terahertz Waves*, 2020, pp. 1–2.
[30] F. D. M. Haldane and S. Raghu, "Possible realization of directional optical waveguides in photonic crystals with broken time-reversal symmetry," *Phys. Rev. Lett.*, vol. 100, no. 1, 2008, Art. no. 013905.
[31] J. W. Dong, X. D. Chen, H. Zhu, Y. Wang, and X. Zhang, "Valley photonic crystals for control of spin and topology," *Nature Mater.*, vol. 16, no. 3, pp. 298–302, 2017.
[32] Z. Gao *et al.*, "Valley surface-wave photonic crystal and its bulk/edge transport," *Phys. Rev. B.*, vol. 96, no. 20, 2017, Art. no. 201402.
[33] F. Gao *et al.*, "Topologically protected refraction of robust kink states in valley photonic crystals," *Nature Phys.*, vol. 4, no. 2, pp. 140–144, 2018.
[34] M. Yan *et al.*, "On-chip valley topological materials for elastic wave manipulation," *Nature Mater.*, vol. 17, no. 11, pp. 993–998, 2018.

[35] X. Wu *et al.*, "Direct observation of valley-polarized topological edge states in designer surface plasmon crystals," *Nature Commun.*, vol. 8, no. 1, pp. 1–9, 2017.
[36] S. Atakaramians, S. Afshar, T. Monro, T. M., and D. Abbott, "Terahertz dielectric waveguides," *Adv. Opt. Photon.*, vol. 5, no. 2, pp. 169–215, 2013.
[37] N. S. Alagha and P. Kabal, "Generalized raised-cosine filters," *IEEE Trans. Commun.*, vol. 47, no. 7, pp. 989–997, Jul. 1999.
[38] V. K. Chinni *et al.*, "Single-channel 100 gbits transmission using III-V UTC-PDs for future IEEE 802.15.3d wireless links in the 300 GHz band," *Electron. Lett.*, vol. 54, no. 10, pp. 638–640, 2018.
[39] ETSI 3rd Generation Partnership Project, "Technical Specification Group Radio Access Network; GSM/EDGE Radio transmission and reception," Release 15, TS 45.005, pp. 1–287, Jun. 2018.
[40] I. Kaminow, T. Li, and A. Wilner, "Optical Fiber Communications," The Netherlands: Elsevier Science, IB New York, NY, USA, 2013.
[41] A. Morello and V. Mignone, "DVB-S2: The second generation standard for satellite broad-band services," *Proc. IEEE*, vol. 94, no. 1, pp. 210–227, Jan. 2006.
[42] Y. Nishida, N. Nishigami, S. Diebold, J. Kim, M. Fujita, and T. Nagatsuma, "Terahertz coherent receiver using a single resonant tunnelling diode," *Sci. Rep.*, vol. 9, no. 1, pp. 1–9, 2019.
[43] X. Yu, J. Y. Kim, M. Fujita, and T. Nagatsuma, "Efficient mode converter to deep-subwavelength region with photonic-crystal waveguide platform for terahertz applications," *Opt. Exp.*, vol. 27, no. 20, pp. 28707–28721, 2019.

Julian Webber (Senior Member, IEEE) received the M.Eng. degree in electronic engineering and the Ph.D. degree in wireless communications from the University of Bristol, Bristol, U.K., in 1996 and 2004, respectively. He was employed on DSP & ASIC engineering with Texas Instruments Europe during 1996–1998 and was engaged during 2001–2007, as a Research Fellow with the University of Bristol, on 4G wireless communications. During 2007–2012, he continued research on MIMO communications with the Graduate School of Information Science and Technology, Hokkaido University, Sapporo, Japan. During 2012–2018, he was employed as a Research Scientist with Advanced Telecommunications Research Institute International, Kyoto, Japan, focusing on spectrally efficient satellite and WLAN systems, serving as a Member of the Japanese technical delegation to the ITU-R and IEEE 802.11 Standardization committees. Since 2018, he has been a specially appointed Assistant Professor of information photonics with the Graduate School of Engineering Science, Osaka University, Toyonaka, Japan, conducting research on resonant tunneling diodes, topological photonic crystals, and new technologies for 6G communications. His research interests include wireless communications, signal processing, and photonic systems for 6G.

Yuichiro Yamagami received the master's degree in engineering science from Osaka University, Osaka, Japan, in 2021. His research was topological photonics and photonic crystals, with special focus on valley photonic crystals in the THz band.

Guillaume Ducournau (Member, IEEE) received the Diplome d'ingénieur degree from ESIGELEC, Rouen, France, in 2002 and the Ph.D. degree in fiber optic communication systems using DPSK modulation schemes from the Université de Rouen, Mont-Saint-Aignan, France, in 2005. In 2002, he worked in Montreal, Canada, on the characterization of optical fiber Bragg gratings for core optical networks. From 2007 to 201, he was an Assistant Professor with the Institute of Electronics, Microelectronics and Nanotechnology (IEMN), University of Lille 1, Villeneuve d'Ascq, France, and the THz Photonics Group, Polytech'Lille Graduate School, where he has been a Full Professor since 2018. He is the Leader of the THz wireless communications activity with IEMN using optoelectronic THz photomixers, electronic receivers, THz instrumentation, and millimeter-wave (mm-wave) characterization. He worked on several ANR and European projects (ITN MITEPHO and STREP ROOTHz). From 2014 to 2017, he was the Co-ordinator of the COM'TONIQ Project, funded by ANR (INFRA 2013) dedicated to THz communications in the 300-GHz band and the ERA-NET TERALINKS Program, in which the main goal is the achievement of THz system level demonstrators based on advanced technologies in the 220-320-GHz range. He coordinates and the ANR/DFG TERASONIC Project for the use of THz photonics technologies and electrical solid-state technologies toward a complete 300-GHz transmission system for 100-Gb/s wireless links and the SPATIO-TERA ANR project for spatially distributed THz sources. He is also participating in the H2020 EU-Japan ThOR project, dedicated to the development of km-range super-heterodyne THz transmission systems compliant to the new IEEE 802.15.3 d standard. He has authored or coauthored more than 140 publications in peer-reviewed international journals or peer-reviewed conferences proceedings and holds one patent.

Pascal Szriftgiser (Senior Member, IEEE) received the Ph.D. degree in quantum physics from the University Paris VI, Laboratoire Kastler Brossel, Paris, France, in 1996. He then joined the Laboratory PhLAM (Physique des Lasers Atomes et Molécules), as a Researcher (CNRS, Centre National de la Recherche Scientifique). He is currently a CNRS Research Director, the Leader of Cold Atoms Group, and the Deputy Director of Laboratory PhLAM. His expertise spans from cold atoms physics, quantum chaos, non-linear optics in optical fibers to high speed coherent optical communications for THz applications. He is the coauthor of more than 70 publications in peer-reviewed journals.

Kei Iyoda is a Master course student with the Graduate School of Engineering Science, Osaka University, Toyonaka, Japan. His research interests include topological photonics and photonic crystals, especially valley photonic crystals.

Masayuki Fujita (Member, IEEE) received the Ph.D. degree from Yokohama National University, Yokohama, Japan, on ultrasmall and ultralow- threshold microdisk lasers, in 2002. Subsequently, he joined the Department of Electronic Science and Engineering, Kyoto University, Kyoto, Japan, and initiated research on photonic crystals, including spontaneous emission control in photonic crystals and high- efficiency light extraction in light-emitting diodes and silicon light emitters. Next, he moved to Osaka University, Toyonaka, Japan, and was appointed the Research Director of the strategic basic research program CREST, Development of terahertz integrated technology platform through fusion of resonant tunneling diodes and photonic crystals of the Japan Science and Technology Agency. He is currently an Associate Professor with the Graduate School of Engineering Science, Osaka University. His research interests include terahertz materials and devices, photonic nanostructures and microstructures, and their applications. He is a Member of the Japan Society of Applied Physics, the Laser Society of Japan, the Institute of Electronics, Information and Communication Engineers (IEICE), Japan, and the Japanese Photochemistry Association. From 1999 to 2002 and from 2003 to 2006, he was a Research Fellow of the Japan Society for the Promotion of Science. He is currently an Associate Editor for the *Applied Physics Express*, and a Chair of the Technical Group on Terahertz Application Systems of IEICE, Japan.

Tadao Nagatsuma (Fellow, IEEE) received the B.S., M.S., and Ph.D. degrees in electronic engineering from Kyushu University, Fukuoka, Japan, in 1981, 1983, and 1986, respectively. In 1986, he joined Electrical Communications Laboratories, Nippon Telegraph and Telephone Corporation (NTT), Atsugi, Kanagawa, Japan. From 1999 to 2002, he was a Distinguished Technical Member with NTT Telecommunications Energy Laboratories. From 2003 to 2007, he was a Group Leader with NTT Microsystem Integration Laboratories and was an NTT Research Professor from 2007 to 2009. Since 2007, he has been with Osaka University, Toyonaka, Osaka, Japan, where he is currently a Professor with the Division of Advanced Electronics and Optical Science, Department of Systems Innovation, Graduate School of Engineering Science.

His research interests include ultrafast electronics and millimeter-wave and terahertz photonics. Dr. Nagatsuma is a Fellow of the Institute of Electronics, Information and Communication Engineers (IEICE), Japan, and a Fellow of the Electromagnetics Academy. He is currently a Track Editor of the IEEE PHOTONICS TECHNOLOGY LETTERS and the *IEEE Transactions on Terahertz Science and Technology*, and a Vice President of the IEICE and the Terahertz Systems Consortium. He was the recipient of numerous awards, including the 1989 IEICE Young Engineers Award, the 1992 IEEE Andrew R. Chi Best Paper Award, the 1997 Okochi Memorial Award, the 1998 Japan Microwave Prize, the 2000 Ministers Award of the Science and Technology Agency, the 2002 and 2011 Asia-Pacific Microwave Conference Prize, the 2004 Yokosuka Research Park Award, the 2006 Asia-Pacific Microwave Photonics Conference Award, the 2006 European Microwave Conference Prize, the 2007 Achievement Award presented by the IEICE, the 2008 Maejima Award, the 2011 Recognition from Kinki Bureau of Telecommunications, Ministry of Internal Affairs and Communications, the 2011 Commendation for Science and Technology by the Ministry of Education, Culture, Sports, Science and Technology, the 2014 IEEE Tatsuo Ito Award, and the 2020 Distinguished Achievement and Contributions Award by the IEICE.

Ranjan Singh (Member, IEEE) is an Indian Scientist born at Jamshedpur in 1978. He received the B.Eng. degree in telecommunications from Bangalore University, India, in 2001, the M.Tech. degree in photonics from the Cochin University of Science and Technology, in Kochi, India, in 2004, and the Ph.D. degree in photonics from the School of Electrical and Computer Engineering, Oklahoma State University, in Stillwater, OK, USA, in 2009. In 2009, he joined Los Alamos National Laboratory, as a Postdoctoral Scientist and worked there till 2013. He founded *TeraX* Labs, in 2013 with the Division of Physics, Nanyang Technological University (NTU), Singapore. He made pioneering contributions to the field of terahertz science and technology for metamaterial sensing, ultrafast switching, and communication applications. His current research interests include terahertz electronic-photonic hybrid technologies for 6G communications, intelligent metasurfaces for beamforming, massive THz-MIMO, biosensors, quantum and nanotechnologies, and light induced high temperature superconductivity. He has raised US$12 M in competitive research grants including US$6.8 M Singapore NRF-CRP23-2019-0005 grant to develop on-chip terahertz topological photonics for 6G communication (TERACOMM). Since 2020, he has been listed as the top 1% highly cited Researcher in the world by the web of science.